The Cosmic-ray Boron Flux Measured from 8.4 GeV/n to 3.8 TeV/n
with the Calorimetric Electron Telescope
on the International Space Station
SUPPLEMENTAL MATERIAL

(CALET collaboration)

Supplemental material concerning "The Cosmic-ray Boron Flux Measured from 8.4 GeV/n to 3.8 TeV/n with the Calorimetric Electron Telescope on the International Space Station".

ADDITIONAL INFORMATION ON THE DATA ANALYSIS

Trigger. The high-energy (HE) trigger efficiency was measured directly from the flight data (FD) by using dedicated runs where in addition to HE, a low-energy (LE) trigger was active. The trigger logic is the same for both triggers (i.e. coincidence of the pulse heights of the last two pairs of IMC layers and the top TASC layer) but lower discriminator thresholds are set for the input signals in the case of the LE trigger, allowing the instrument to trigger on penetrating nuclei with $Z > 2$. The ratio of the number of events counted by both triggers to those recorded by the LE trigger alone is an estimate of the HE trigger efficiency in each bin of deposited energy. The HE trigger efficiency curves as a function of the total deposited energy in the TASC (E_{TASC}) are shown in Fig. S1, where they are compared with MC simulations in which both trigger modes are modeled. The FD trigger curves are in good agreement with the MC predictions, the average difference being -0.5% for B and -0.7% for C.

Charge identification. The identification of the particle charge Z is based on the measurements of the ionization deposits in the CHD and IMC. The particle trajectory makes it possible to locate the CHD paddles and IMC fibers traversed by the primary particle and to determine the path length correction to the signals for the extraction of the dE/dx samples. Three independent dE/dx measurements are obtained, one for each CHD layer and the third one by averaging the samples (at most eight) along the track in the upper half of the IMC, summing up the signals of the crossed fiber in each layer and its two neighbors. In order to suppress the contribution of possible signals of secondary tracks wrongly associated to the track of the primary nucleus, only dE/dx signals larger than 1.5 MeV/mm (corresponding to the energy released in a fiber by 10 MIPs (Minimum Ionizing Particles)) are used in the mean calculation.

Calibration curves of dE/dx are built by fitting FD subsets for each nuclear species to a function of Z^2 by using a "halo" model [S1], in which dE/dx is parametrized as the sum of two contributions ("core" and "halo", respectively)

$$\frac{dE}{dx} = \frac{A(1-f_h)\alpha Z^2}{1 + B_S(1-f_h)\alpha Z^2 + C_S\alpha^2 Z^4} + Af_h\alpha Z^2 \tag{S1}$$

where the parameter f_h represents the fraction of energy deposited in the halo; B_S and C_S model the strength of the scintillation quenching; A is an overall normalization constant; and α is close to 2 MeV g^{-1} cm^2 for a plastic scintillator. The parameters are extracted from the fits separately for the CHDX, CHDY and IMC. These three calibration curves are then used to reconstruct three charge values (Z_{CHDX}, Z_{CHDY}, Z_{IMC}) from the measured dE/dx yields on an event-by-event basis. For high-energy showers, the charge peaks are corrected for a systematic shift to higher values (up to 0.15 e) with respect to the nominal charge positions, due to the large amount of shower particle tracks backscattered from the TASC whose signals add up to the primary particle ionization signal. The resulting distribution of the reconstructed charge (Z_{CHD}) combining Z_{CHDX} and Z_{CHDY} is shown in Fig. S2(a). B and C candidates are selected by applying a window cut of half-width 0.45 centered on the nominal charge values ($Z = 5, 6$). Events with C nuclei undergoing a charge-changing nuclear interaction at the top of the IMC are clearly visible in the tail of the C drop-shaped distribution extending to lower Z_{IMC} values in Fig. S2(b). They are removed by requiring consistency between the CHD and IMC charges ($|Z_{\text{CHD}} - Z_{\text{IMC}}| < 1$), and among the individual charge values measured in the four upper pairs of adjacent fiber layers.

Track width. A clustering algorithm is applied to the fibers being hit in the IMC before track finding and fitting. In each IMC layer, neighboring fibers with an energy deposit >0.3 MIPs are clustered around the fibers with larger signals. The position of each cluster is computed as the center-of-gravity (COG) of its fibers. The cluster positions are taken as candidate track points for the combinatorial Kalman filter algorithm [S2] which is used to identify the clusters associated to the primary particle track and to reconstruct its direction and entrance point at the top of the instrument. In each layer l, we define the track width as

$$\text{TW}_l = \frac{\sum\limits_{j=m-3}^{m+3} E_{l,j} - \sum\limits_{j=m-1}^{m+1} E_{l,j}}{Z_l^2} \tag{S2}$$

where $E_{l,j}$ is the energy deposit in the fiber j of the layer l, m is the index of the fiber with the maximum signal in the cluster crossed by the primary particle track, and the numerator represents the difference between the total energy deposited in the 7 central fibers of the cluster and the cluster core, made of 3 fibers. Z_l is the charge in the layer l which is calculated by using the signals of the 5 central fibers in the cluster crossed by the track. The total

track width is then defined as

$$\mathrm{TW} = \frac{1}{6}\sum_{l=1}^{6}\mathrm{TW}_l \qquad (S3)$$

where the sum is limited to the first eight IMC layers from the top excluding the two layers with maximum and minimum Z_l, respectively.

The TW of interacting events at the top of the instrument is wider than that of penetrating nuclei, due to the angular spread of secondary particles produced in the interaction and their lower specific ionization compared to that of the primary particle. In Fig. S3, a sample of B events selected in FD by means of the CHD only (i.e. without the IMC consistency cuts described above) is compared with the distributions obtained from MC simulations of B and other nuclei, applying the same selections as for FD. It can be noticed that B nuclei traversing CHD and the top of the IMC without interacting show a peak at low TW values (red filled histogram), while the broad distribution at large TW values is due to the interaction of background particles (mainly protons, He, C) misidentified as boron (blue filled histogram). A cut on TW < 0.18 is applied to select penetrating B events and reject both early interacting B nuclei (the right-hand tail in the red filled histogram) and the background from other nuclear species.

Studying TW distributions similar to the ones shown in Fig. S3 but obtained by applying also the IMC consistency cuts, a residual background contamination can be computed as the fraction of nuclei misidentified as B and not rejected by the TW cut, compared to the number of selected B events in different intervals of E_{TASC}. This contamination fraction is $\sim 1\%$ for $E_{\mathrm{TASC}} < 10^2$ GeV and grows logarithmically for $E_{\mathrm{TASC}} > 10^2$ GeV, approaching $\sim 7\%$ at 1.5 TeV. The estimated E_{TASC} distribution of the background in the final B sample is shown in Fig. S4 as a blue-filled histogram. It is subtracted from the B distribution in FD (red-filled histogram) before the application of the unfolding procedure.

Selection efficiency. The efficiency of the complete selection procedure of B and C nuclei, estimated from MC and including trigger, tracking, charge identification and TW efficiencies, is shown as a function of the kinetic energy per nucleon in Fig. S5.

Systematic uncertainties. The flux systematic relative errors stemming from several sources, including HE trigger efficiency, charge identification, MC simulations, energy scale, energy unfolding, background contamination, and live time are shown in Fig. S6 as a function of the kinetic energy per nucleon. The dominant source of uncertainty in the flux derives from the different predictions of the energy response matrix by simulations based on EPICS and Geant4. Energy-independent systematic uncertainties affecting the flux normalization include live time (3.4%), long-term stability of charge calibration (0.5%), energy scale calibration (3%), and assumption of the B isotopic composition (1.7%). With the exception of the latter, the other energy-independent systematic uncertainties cancel out completely in the B/C ratio.

Additional systematic effects that have been studied extensively are related to the particle interactions in the materials of the instrument. Primary particles cross a 2 mm-think Al panel covering the top of the instrument, before reaching the CHD. The probability of interactions of B and C nuclei in this panel is $\lesssim 1\%$. This effect is taken into account in the flux calculation.

CR nuclei traverse several materials in the IMC, mainly composed of CFRP (Carbon Fiber Reinforced Polymer), aluminum and tungsten. Possible uncertainties in the inelastic cross sections in MC simulations or discrepancies in the material description might affect the flux normalization. We have checked that hadronic interactions are well simulated in the detector, by measuring the survival probabilities of C nuclei at different depths in the IMC. The survival probabilities are in agreement with MC prediction within <1% as shown in Fig. S7.

Several studies were performed to check the stability of the detector performance. Day-by-day calibrations of the detector channels are performed by using penetrating protons and He particles selected by a dedicated trigger mode. This ensures that the CHD and IMC charge measurements are stable over time at the level of 0.5%.

To investigate the uncertainty in the definition of the acceptance, restricted acceptance (up to 20% of the nominal one) regions were also studied. The corresponding fluxes are consistent within statistical fluctuations.

To investigate possible time-dependent effects in the energy scale of the TASC, we have compared C flux measurements obtained with subsets of data taken in different periods of time. We have chosen for comparison an energy interval between 30 GeV/n and 300 GeV/n, to exclude the low-energy region where the flux is affected by solar modulation and the high-energy region where statistical fluctuations are relevant. In this energy interval, the fluxes in different time periods turned out to be in agreement at a level consistent with the energy scale calibration error (3%).

Energy spectra. The CALET energy spectra of B and C and the B/C flux ratio, together with a compilation of the available data, are shown in Fig. S8, which is an enlarged version of Fig. 2 in the main body of the paper. In tables I and II, the B and C differential fluxes in different energy intervals are reported with the separate contributions to the flux error of the statistical uncertainties, the systematic uncertainties in normalization, and energy dependent systematic uncertainties. The data of the B/C flux ratio are reported in table III.
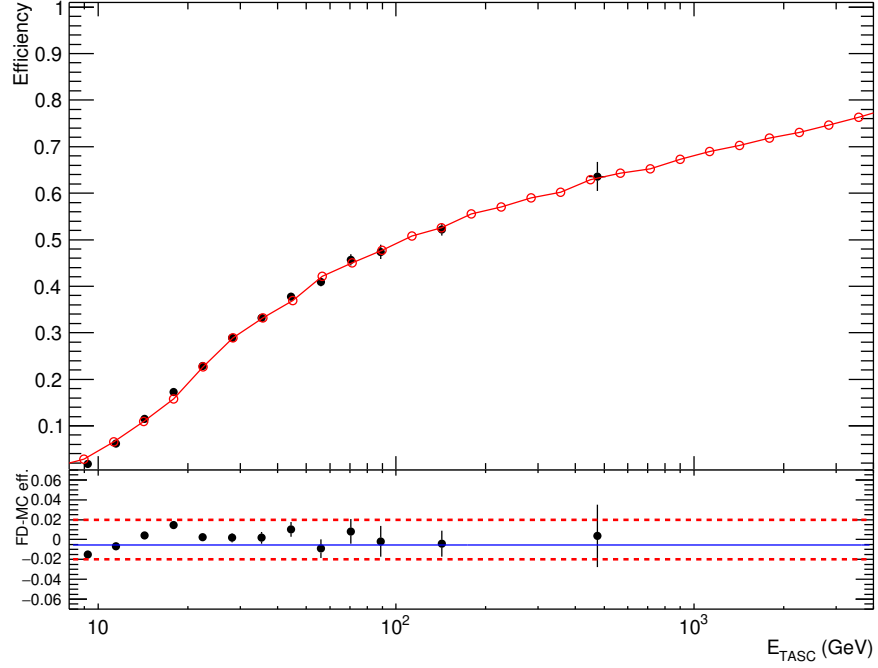
(a)
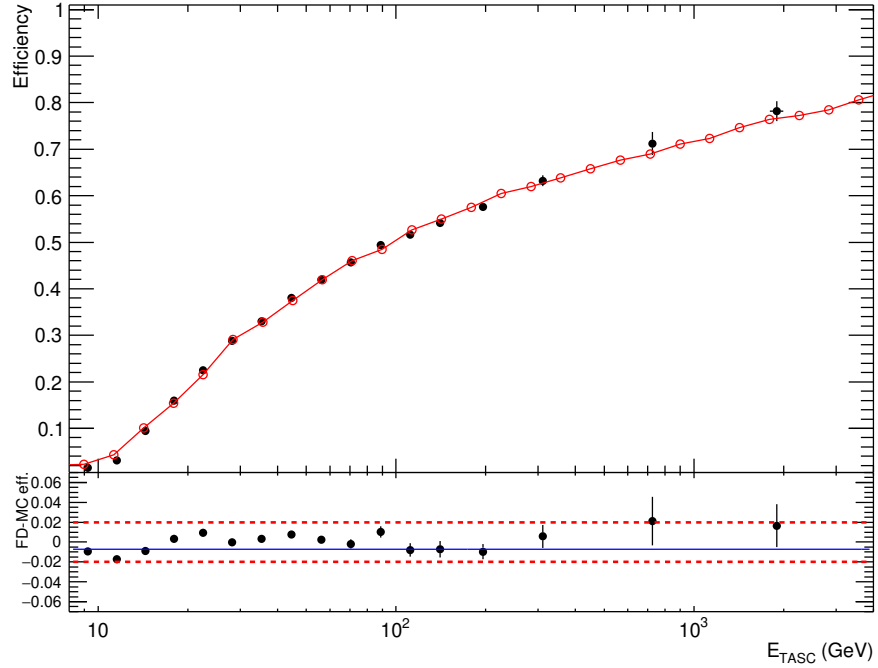
(b)

FIG. S1. HE trigger efficiency as a function of the deposited energy in the TASC for B (a) and C (b) as derived from flight data (FD) (black dots) and Monte Carlo (MC) (red curves). The difference between FD and MC efficiencies is within $\pm 2\%$ over the whole energy range, as shown by the red dotted lines in the bottom plots of panels (a) and (b). The average difference is -0.5% for B and -0.7% for C, as indicated by the blue lines.
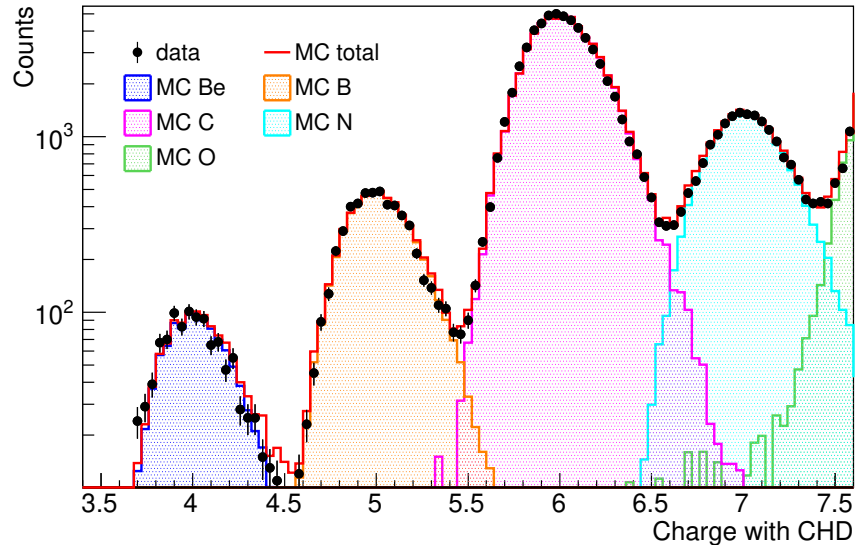
(a)
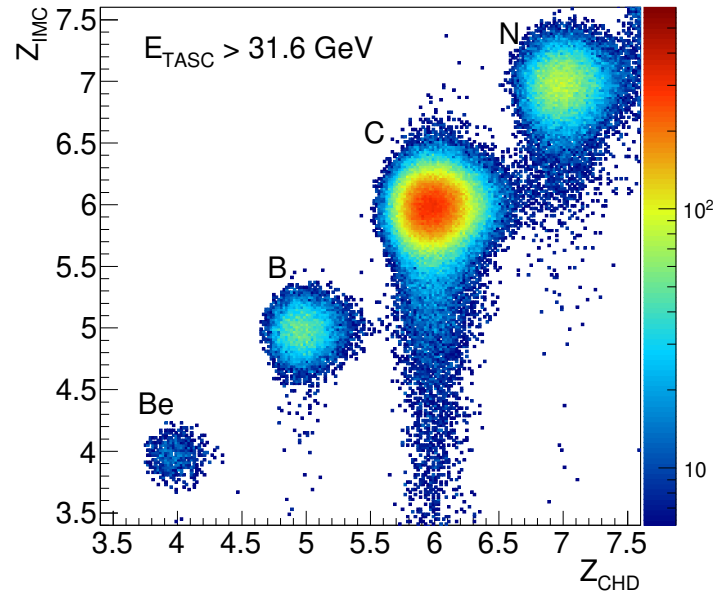
(b)

FIG. S2. (a) Charge distribution measured in the energy interval $100 < E_{\mathrm{TASC}}/\mathrm{GeV} < 215$ by the combined CHD layers (FD, black dots) compared to MC simulations. Events are selected by requiring a measured charge in IMC consistent with Z_{CHD} and a track width TW < 0.18 (Fig. S3). (b) Charge correlation between Z_{IMC} and Z_{CHD} in a sample of FD selected without applying the consistency cuts between CHD and IMC or the TW cut.
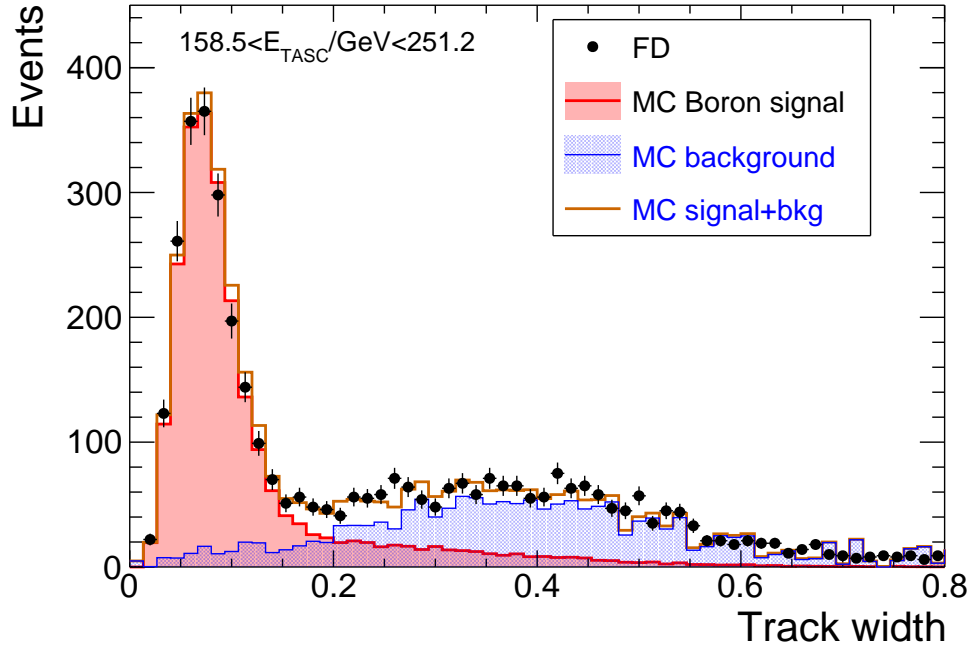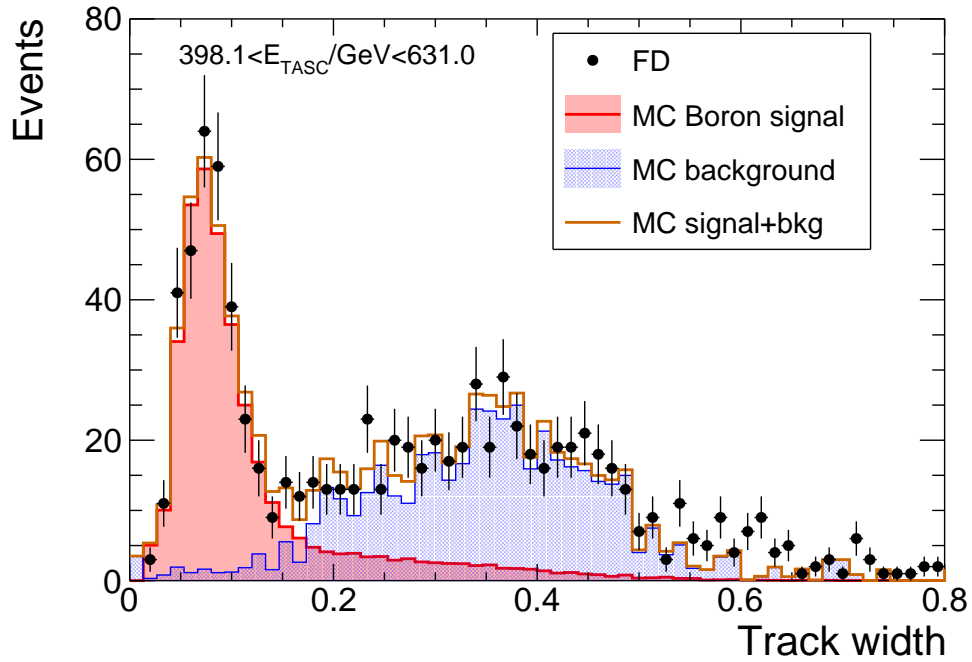
FIG. S3. Distributions of the track width (TW) variable in two different intervals of E_{TASC}. The black dots represent a sample of B events selected in FD by means of the CHD only. MC distributions of B and other background nuclei (mainly proton, He, C) are obtained with the same selections used for FD.
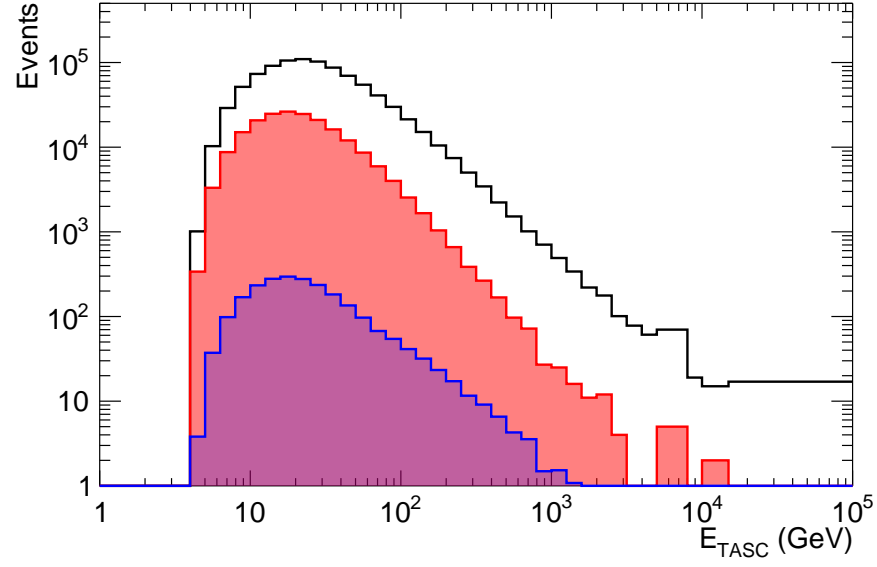
FIG. S4. Distribution of total deposited energy in the TASC for the final selection of carbon (black histogram) and boron (red histogram) candidates in FD. The blue-filled histogram represents the background contamination subtracted from the B sample for the flux measurement.
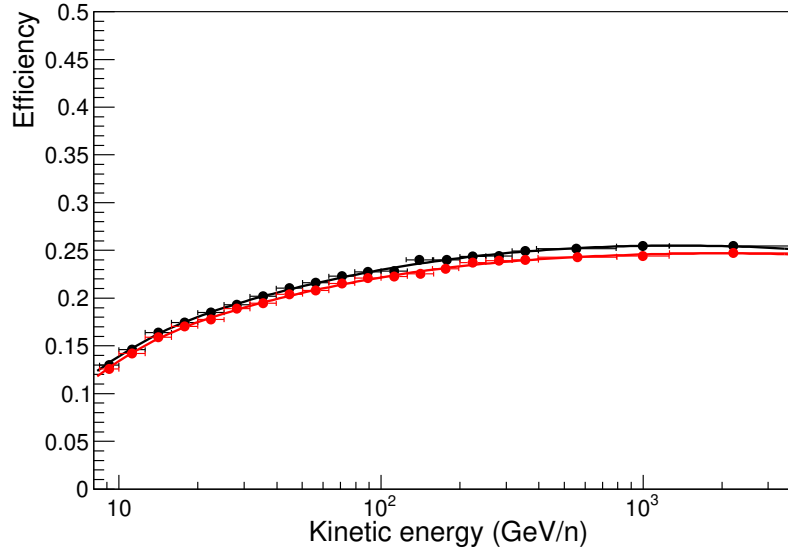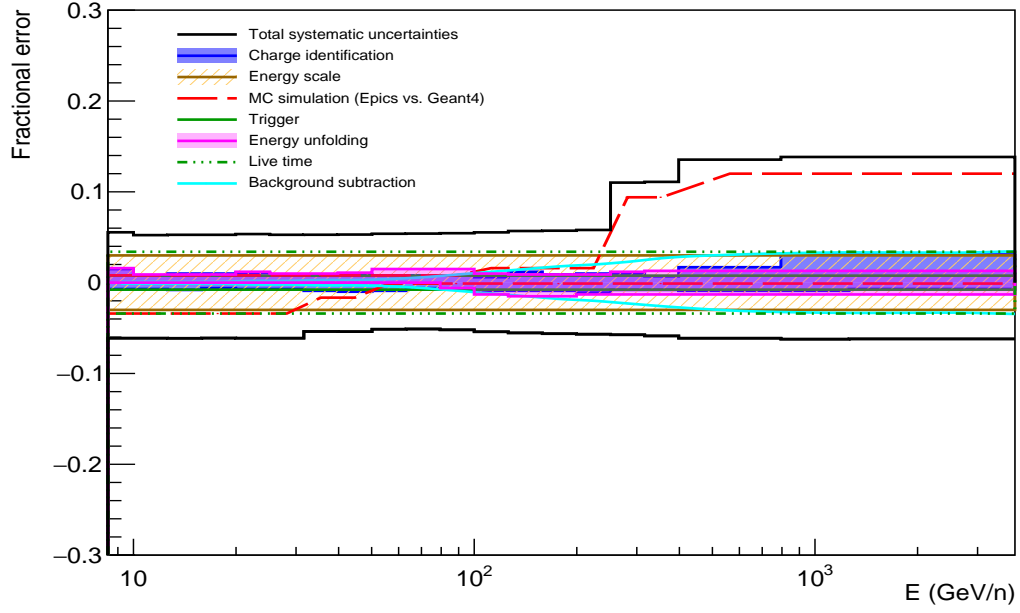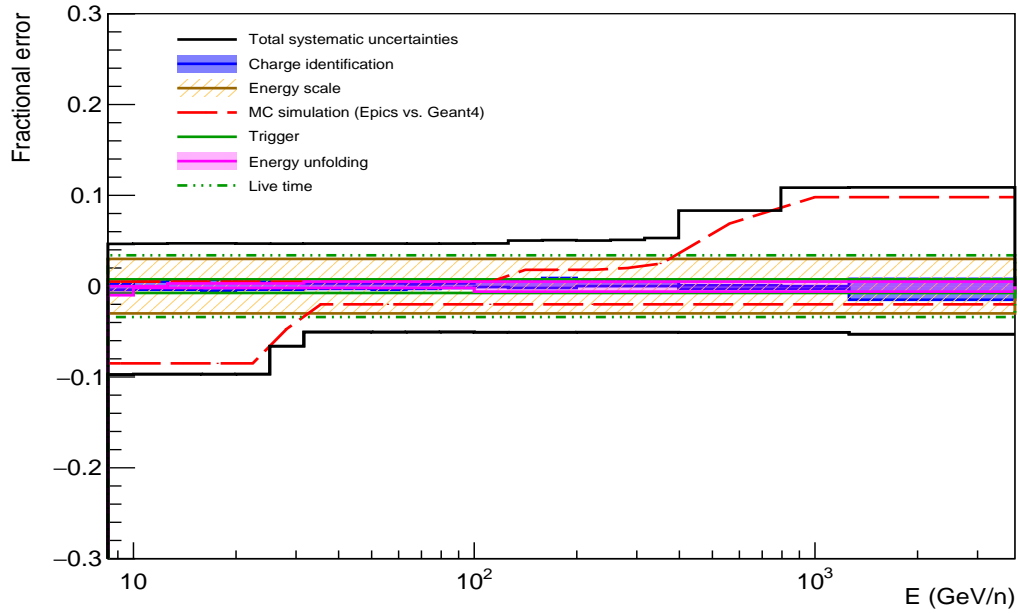

FIG. S5. Total selection efficiency for B (red dots) and C (black dots) estimated with MC simulations.

(a)

(b)

FIG. S6. Energy dependence of systematic uncertainties (relative errors) for B (*a*) and C (*b*). The band within the black lines shows the sum in quadrature of all the sources of systematics. A detailed breakdown of systematic errors stemming from charge identification, HE trigger, MC simulations, energy scale, energy unfolding, background contamination, live time is shown.
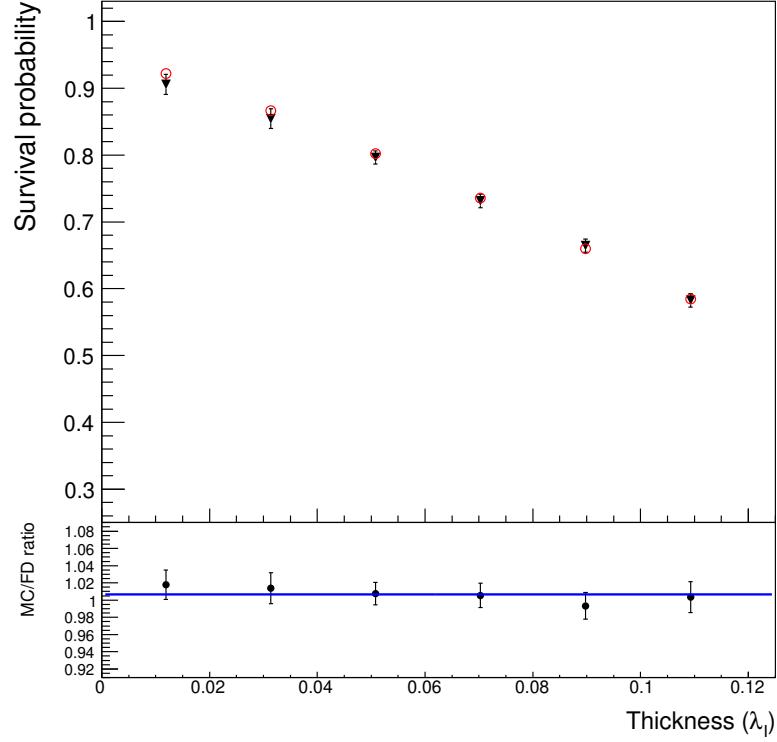
FIG. S7. Survival probability as a function of the material thickness traversed by C nuclei in the IMC as derived from FD (black triangles) and MC (red circles). The survival probabilities are calculated in FD by dividing the number of events selected as C in the first six double layers of scintillating fibers in the IMC by the number of C events selected with the CHD. The material thickness is expressed in units of proton interaction length λ_I and it is measured from the bottom of the CHD. The double fiber layers are preceded by 0.2 X_0-thick W plates (except the first pair), Al honeycomb panels and CFRP supporting structures. In the bottom panel, the blue line represents a constant value fitted to the ratio between MC and FD survival probabilities. The fitted value is 1.006 ± 0.006.
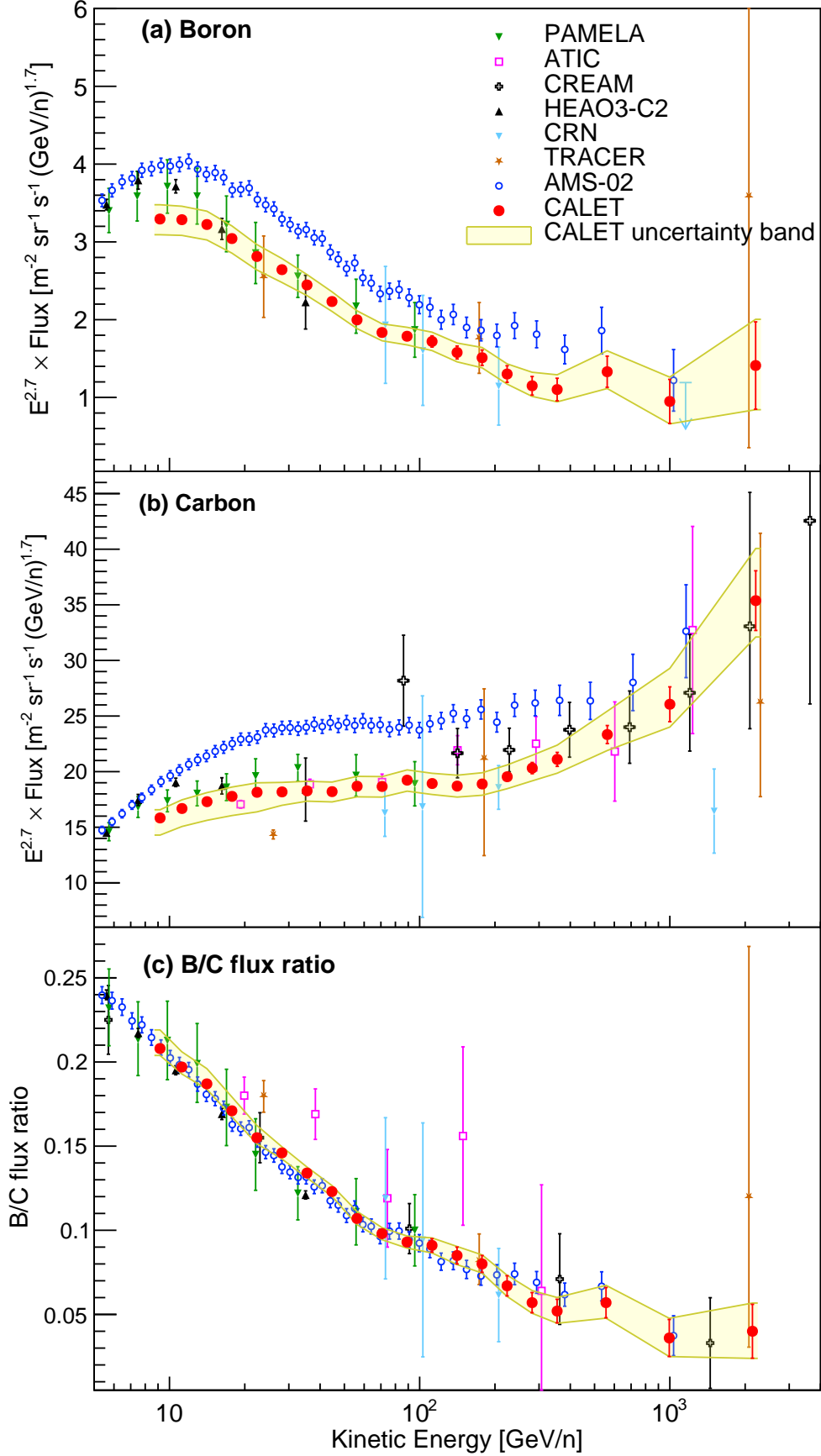
FIG. S8. CALET (a) boron and (b) carbon flux (multiplied by $E^{2.7}$) and (c) ratio of boron to carbon, as a function of kinetic energy E. Error bars of CALET data (red) represent the statistical uncertainty only, while the yellow band indicates the quadratic sum of statistical and systematic errors. Also plotted are other direct measurements [S3–S11].

TABLE I. Table of CALET boron spectrum. The first, second and third errors in the flux represent the statistical uncertainties, systematic uncertainties in normalization, and energy dependent systematic uncertainties, respectively.

Energy Bin [GeV/n]	Flux [m^{-2}sr^{-1}s^{-1}(GeV/n)$^{-1}$]
8.4–10.0	$(8.313 \pm 0.045 \pm 0.405\,^{+0.221}_{-0.307}) \times 10^{-3}$
10.0–12.6	$(4.811 \pm 0.029 \pm 0.234\,^{+0.092}_{-0.178}) \times 10^{-3}$
12.6–15.8	$(2.535 \pm 0.018 \pm 0.123\,^{+0.051}_{-0.094}) \times 10^{-3}$
15.8–20.0	$(1.285 \pm 0.011 \pm 0.063\,^{+0.026}_{-0.047}) \times 10^{-3}$
20.0–25.1	$(6.379 \pm 0.065 \pm 0.311\,^{+0.142}_{-0.236}) \times 10^{-4}$
25.1–31.6	$(3.219 \pm 0.039 \pm 0.157\,^{+0.065}_{-0.119}) \times 10^{-4}$
31.6–39.8	$(1.600 \pm 0.024 \pm 0.078\,^{+0.033}_{-0.037}) \times 10^{-4}$
39.8–50.1	$(7.846 \pm 0.142 \pm 0.382\,^{+0.164}_{-0.182}) \times 10^{-5}$
50.1–63.1	$(3.768 \pm 0.085 \pm 0.183\,^{+0.087}_{-0.060}) \times 10^{-5}$
63.1–79.4	$(1.859 \pm 0.052 \pm 0.091\,^{+0.044}_{-0.028}) \times 10^{-5}$
79.4–100.0	$(9.723 \pm 0.335 \pm 0.473\,^{+0.237}_{-0.176}) \times 10^{-6}$
100.0–125.9	$(5.026 \pm 0.210 \pm 0.245\,^{+0.133}_{-0.118}) \times 10^{-6}$
125.9–158.5	$(2.476 \pm 0.130 \pm 0.121\,^{+0.073}_{-0.065}) \times 10^{-6}$
158.5–199.5	$(1.273 \pm 0.083 \pm 0.062\,^{+0.038}_{-0.036}) \times 10^{-6}$
199.5–251.2	$(5.889 \pm 0.483 \pm 0.287\,^{+0.186}_{-0.172}) \times 10^{-7}$
251.2–316.2	$(2.795 \pm 0.290 \pm 0.136\,^{+0.276}_{-0.085}) \times 10^{-7}$
316.2–398.1	$(1.438 \pm 0.189 \pm 0.070\,^{+0.143}_{-0.047}) \times 10^{-7}$
398.1–794.3	$(5.010 \pm 0.753 \pm 0.244\,^{+0.633}_{-0.186}) \times 10^{-8}$
794.3–1258.9	$(7.553 \pm 2.253 \pm 0.368\,^{+0.978}_{-0.292}) \times 10^{-9}$
1258.9–3860.5	$(1.328 \pm 0.528 \pm 0.065\,^{+0.172}_{-0.051}) \times 10^{-9}$

TABLE II. Table of CALET carbon spectrum. The first, second and third errors in the flux represent the statistical uncertainties, systematic uncertainties in normalization, and energy dependent systematic uncertainties, respectively.

Energy Bin [GeV/n]	Flux [m^{-2}sr^{-1}s^{-1}(GeV/n)$^{-1}$]
8.4–10.0	$(3.990 \pm 0.010 \pm 0.182\,^{+0.037}_{-0.343}) \times 10^{-2}$
10.0–12.6	$(2.440 \pm 0.006 \pm 0.111\,^{+0.025}_{-0.208}) \times 10^{-2}$
12.6–15.8	$(1.358 \pm 0.004 \pm 0.062\,^{+0.016}_{-0.116}) \times 10^{-2}$
15.8–20.0	$(7.496 \pm 0.026 \pm 0.342\,^{+0.088}_{-0.641}) \times 10^{-3}$
20.0–25.1	$(4.108 \pm 0.016 \pm 0.187\,^{+0.044}_{-0.351}) \times 10^{-3}$
25.1–31.6	$(2.211 \pm 0.010 \pm 0.101\,^{+0.023}_{-0.106}) \times 10^{-3}$
31.6–39.8	$(1.193 \pm 0.006 \pm 0.054\,^{+0.013}_{-0.026}) \times 10^{-3}$
39.8–50.1	$(6.385 \pm 0.040 \pm 0.291\,^{+0.069}_{-0.138}) \times 10^{-4}$
50.1–63.1	$(3.520 \pm 0.025 \pm 0.161\,^{+0.038}_{-0.077}) \times 10^{-4}$
63.1–79.4	$(1.888 \pm 0.016 \pm 0.086\,^{+0.020}_{-0.041}) \times 10^{-4}$
79.4–100.0	$(1.045 \pm 0.011 \pm 0.048\,^{+0.011}_{-0.023}) \times 10^{-4}$
100.0–125.9	$(5.523 \pm 0.067 \pm 0.252\,^{+0.063}_{-0.123}) \times 10^{-5}$
125.9–158.5	$(2.930 \pm 0.043 \pm 0.134\,^{+0.062}_{-0.065}) \times 10^{-5}$
158.5–199.5	$(1.589 \pm 0.028 \pm 0.073\,^{+0.035}_{-0.035}) \times 10^{-5}$
199.5–251.2	$(8.830 \pm 0.186 \pm 0.403\,^{+0.185}_{-0.196}) \times 10^{-6}$
251.2–316.2	$(4.931 \pm 0.122 \pm 0.225\,^{+0.112}_{-0.109}) \times 10^{-6}$
316.2–398.1	$(2.750 \pm 0.082 \pm 0.125\,^{+0.074}_{-0.061}) \times 10^{-6}$
398.1–794.3	$(8.770 \pm 0.305 \pm 0.400\,^{+0.610}_{-0.196}) \times 10^{-7}$
794.3–1258.9	$(2.070 \pm 0.124 \pm 0.094\,^{+0.204}_{-0.046}) \times 10^{-7}$
1258.9–3860.5	$(3.325 \pm 0.252 \pm 0.152\,^{+0.328}_{-0.089}) \times 10^{-8}$

TABLE III. Table of CALET boron to carbon flux ratio. The first and second errors represent the statistical uncertainties and systematic uncertainties, respectively.

Energy Bin [GeV/n]	B/C
8.4–10.0	$0.208 \pm 0.001 ^{+0.011}_{-0.004}$
10.0–12.6	$0.197 \pm 0.001 ^{+0.009}_{-0.004}$
12.6–15.8	$0.187 \pm 0.001 ^{+0.009}_{-0.003}$
15.8–20.0	$0.171 \pm 0.002 ^{+0.008}_{-0.003}$
20.0–25.1	$0.155 \pm 0.002 ^{+0.007}_{-0.003}$
25.1–31.6	$0.146 \pm 0.002 ^{+0.003}_{-0.003}$
31.6–39.8	$0.134 \pm 0.002 ^{+0.003}_{-0.002}$
39.8–50.1	$0.123 \pm 0.002 ^{+0.003}_{-0.002}$
50.1–63.1	$0.107 \pm 0.003 ^{+0.003}_{-0.002}$
63.1–79.4	$0.098 \pm 0.003 ^{+0.002}_{-0.002}$
79.4–100.0	$0.093 \pm 0.003 ^{+0.002}_{-0.002}$
100.0–125.9	$0.091 \pm 0.004 ^{+0.002}_{-0.002}$
125.9–158.5	$0.085 \pm 0.005 ^{+0.002}_{-0.002}$
158.5–199.5	$0.080 \pm 0.005 ^{+0.002}_{-0.002}$
199.5–251.2	$0.067 \pm 0.006 ^{+0.002}_{-0.002}$
251.2–316.2	$0.057 \pm 0.006 ^{+0.004}_{-0.002}$
316.2–398.1	$0.052 \pm 0.007 ^{+0.004}_{-0.002}$
398.1–794.3	$0.057 \pm 0.009 ^{+0.005}_{-0.002}$
794.3–1258.9	$0.036 \pm 0.011 ^{+0.004}_{-0.001}$
1258.9–3860.5	$0.040 \pm 0.016 ^{+0.005}_{-0.002}$

[S1] P. S. Marrocchesi *et al.*, Nucl. Instr. and Meth. A **659**, 477 (2011).
[S2] P. Maestro and N. Mori (CALET), in *Proceedings of Science (ICRC2017) 208* (2017).
[S3] J. J. Engelmann *et al.* (HEAO-3), Astron. Astrophys. **233**, 96 (1990).
[S4] S.P. Swordy *et al.*, Astrophys. J. **349**, 625 (1990).
[S5] H. S. Ahn *et al.* (CREAM), Astroparticle Phys. **30**, 133 (2008).
[S6] A. Obermeier *et al.* (TRACER), Astrophys. J. **752**, 69 (2012).
[S7] O. Adriani *et al.* (PAMELA), Astrophys. J. **93**, 791 (2014).
[S8] M. Aguilar *et al.* (AMS), Physics Reports **894**, 1 (2021).
[S9] M. Aguilar *et al.* (AMS), Phys. Rev. Lett. **120**, 021101 (2018).
[S10] A. Panov *et al.* (ATIC), Bull. Russian Acad. Sci. **73**, 564 (2009).
[S11] H. S. Ahn *et al.* (CREAM), Astrophys. J. **707**, 593 (2009).